WATER

Probing structural superlubricity of two-dimensional water transport with atomic resolution

Da Wu[1]†, Zhengpu Zhao[1]†, Bo Lin[2]†, Yizhi Song[1]†, Jiajie Qi[3]†, Jian Jiang[2], Zifeng Yuan[1], Bowei Cheng[1], Mengze Zhao[3], Ye Tian[1], Zhichang Wang[1], Muhong Wu[1,4,5], Ke Bian[1], Kai-Hui Liu[3,4,6]*, Li-Mei Xu[1,4,6]*, Xiao Cheng Zeng[2,7]*, En-Ge Wang[1,4,5,8]*, Ying Jiang[1,4,6,9]*

Low-dimensional water transport can be drastically enhanced under atomic-scale confinement. However, its microscopic origin is still under debate. In this work, we directly imaged the atomic structure and transport of two-dimensional water islands on graphene and hexagonal boron nitride surfaces using qPlus-based atomic force microscopy. The lattice of the water island was incommensurate with the graphene surface but commensurate with the boron nitride surface owing to different surface electrostatics. The area-normalized static friction on the graphene diminished as the island area was increased by a power of ~−0.58, suggesting superlubricity behavior. By contrast, the friction on the boron nitride appeared insensitive to the area. Molecular dynamic simulations further showed that the friction coefficient of the water islands on the graphene could reduce to <0.01.

Water transport in low-dimensional materials for nanofluidic devices has recently attracted tremendous attention (1–14). The key interest lies in that the water flow rate could be drastically enhanced when the dimension of the confinement geometry approaches the atomic scale (<1 nm), leading to almost vanishing friction (superlubricity) (1–6). This counterintuitive property has potentially broad applications in desalination (15–17), nanofiltration (6, 11, 18), and energy harvesting (19, 20). The frictionless water transport is best exemplified in the homopolar carbon-based nanomaterials, such as zero-dimensional (0D) nanopores (15, 16), 1D carbon nanotubes (1–5, 11), and 2D channels (10, 12) made from graphene layers. It has been proposed that the superlubricity may arise from the curvature-induced structural incommensurability for the water in 1D carbon nanotubes (21). However, this idea cannot apply to the 2D graphene channels, where no curvature effect is present. So far, our understanding of the frictionless water transport under atomic confinement is still elusive.

Notably, for isostructural but heteropolar hexagonal boron nitride (hBN) materials, there exists much larger water friction, and no slip is detected. It has been shown that the graphite capillaries exhibit nearly two orders of magnitude–higher fluxes than the hBN devices under atomic-scale confinement (22). Considering that the graphene and hBN surfaces have a minute lattice difference of ~1.8% (23) and yield similar contact angles of water droplets (24), such a striking difference of water transport in these two materials is way beyond current theoretical expectations, which have revealed that the water friction on the hBN surface is only three to five times larger than that on the graphene (25, 26). Experimentally, some efforts have been made to evaluate the water slip length (5, 22, 27, 28), but the direct measurement of the water friction and the interfacial water structure with atomic precision has remained a great challenge.

Growth and high-resolution imaging of 2D water on graphene and hBN

It is known that the atomically confined water tends to become structurally ordered or form icelike structures even under ambient conditions (29–34). In light of this fact, we managed to grow 2D water islands in situ on both the hydrophobic graphene and hBN surfaces to mimic the 2D confined water (materials and methods). Using qPlus-based atomic force microscopy (AFM) (materials and methods) (35) under 6 K and ultrahigh vacuum, we revealed that the 2D water on the two surfaces had the same bilayer hexagonal icelike structure, which is similar to that of the water strongly confined between the hydrophobic sheets with subnanometer spacing (31, 36, 37). Despite the structural similarity, we found that the 2D water islands had different commensurability with the graphene and hBN surfaces, leading to qualitatively different static friction behav-

ior (superlubricity or not). These results provided the microscopic origin of the frictionless water transport at low dimensions and highlighted the sensitivity of structural superlubricity to the surface electrostatics, which is absent in the previous studies on the conventional solid-on-solid friction (38).

Figure 1 shows the structure of 2D water islands grown on the Cu(111)-supported monolayer graphene and hBN. On the graphene surface, almost all the water islands were attached to the step edges of graphene-Cu(111) with a small island density, and very few water islands existed on the graphene terrace by nucleating at surface defects (Fig. 1A and fig. S1). By contrast, the water could easily nucleate on the terrace of the hBN surface with much higher density (Fig. 1B). Such a difference suggests that the water diffusion on the graphene was much faster than that on the hBN. The AFM image of the graphene surface showed a perfect honeycomb structure (Fig. 1C), and B and N atoms on the hBN surface exhibited different force contrasts (Fig. 1D and fig. S2) (39). The 2D water islands grown on graphene and hBN had the same height (fig. S3) and structure as those grown on Au(111), consisting of two flat hexagonal water layers interlocked together (2D ice phase I; Fig. 1, E and F) (40). Each water molecule formed three hydrogen bonds with in-plane nearest-neighbor water molecules and one hydrogen bond with a water molecule in the opposing plane, leading to saturation of all hydrogen bonds (Fig. 1, G to J). The honeycomb structures in Fig. 1, E and F, basically reflected the oxygen (O) lattices due to the Pauli repulsion force, and the flat and vertical water molecules could be clearly distinguished by probing the higher-order electrostatic force (40, 41), which was sensitive to the water dipole orientation (fig. S4). Such an interlocked-bilayer icelike structure has been also found under the hydrophobic confinement geometry with atomic scale, even at ambient temperatures (29–31).

Determination of the lattice commensurability

Although the overall structure of the 2D water islands was the same on graphene and hBN, the lattice registry of those islands with the two substrates was different. Figure 2A shows the large-scale AFM image of a typical water island on the graphene. We could clearly discern boundary structures within the island. In the zoomed-in AFM image (Fig. 2B), the boundary was resolved to be a line defect, consisting of alternative pentagons and heptagons. The honeycomb water lattices on the two sides of the boundary were rotated 30° with respect to each other. By resolving the atomic lattices of the graphene and the water island in the same image (materials and methods), we were able to precisely superimpose the graphene lattice onto the water island. Carbon hexagons of the

[1]International Center for Quantum Materials, School of Physics, Peking University, Beijing 100871, China. [2]Department of Materials Science and Engineering, City University of Hong Kong, Hong Kong 999077, China. [3]State Key Laboratory for Mesoscopic Physics, Frontiers Science Center for Nano-optoelectronics, School of Physics, Peking University, Beijing 100871, China. [4]Interdisciplinary Institute of Light-Element Quantum Materials and Research Centre for Light-Element Advanced Materials, Peking University, Beijing 100871, China. [5]Songshan Lake Materials Laboratory, Institute of Physics, CAS and School of Physics, Liaoning University, Shenyang 110036, China. [6]Collaborative Innovation Center of Quantum Matter, Beijing 100871, China. [7]Hong Kong Institute for Clean Energy, City University of Hong Kong, Hong Kong 999077, China. [8]Tsientang Institute for Advanced Study, Zhejiang 310024, China. [9]New Cornerstone Science Laboratory, Peking University, Beijing 100871, China.
*Corresponding author. Email: khliu@pku.edu.cn (K.-H.L.); limei.xu@pku.edu.cn (L.-M.X.); xzeng26@cityu.edu.hk (X.C.Z.); egwang@pku.edu.cn (E.-G.W.); yjiang@pku.edu.cn (Y.J.)
†These authors contributed equally to this work.
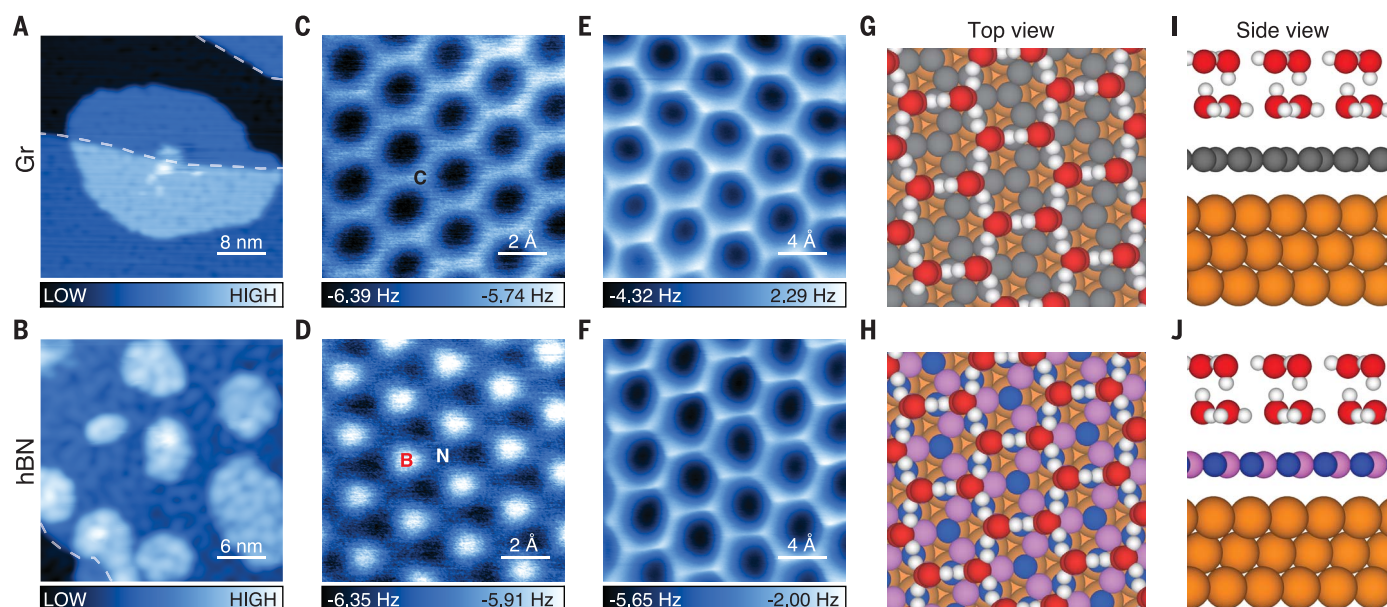
Fig. 1. Atomic structures of the 2D water islands on the graphene and hBN substrates. (**A** and **B**) Constant-current scanning tunneling micrscopy (STM; set point: 60 mV, 3 pA) images of as-grown 2D water islands on the graphene (Gr) (A) and hBN (B) substrates. Step edges of the substrates are denoted by white dashed lines. (**C** and **D**) Constant-height AFM images of the graphene (C) and hBN (D) substrates. C, B, and N atoms are marked in (C) and (D). (**E** and **F**) Constant-height AFM images of the 2D water islands with a hexagonal honeycomb structure on the graphene (E) and hBN (F) substrates. (**G** to **J**) Top and side views of the most-stable 2D water structure on the graphene [(G) and (I)] and hBN [(H) and (J)] substrates obtained by the DFT calculation with commensurate lattices. Cu, O, H, C, B, and N atoms are denoted as orange, red, white, gray, purple, and blue spheres, respectively.

graphene substrate showed no evident registry with water hexagons on the two sides of the boundary (Fig. 2C and fig. S5). Therefore, the water island was incommensurate with the graphene surface.

The 2D water islands grown on the hBN also showed boundary structures, but with a larger width than those on the graphene (Fig. 2D). The high-resolution AFM image revealed that the boundary structure consisted of multiple pentagons, hexagons, heptagons, and octagons (Fig. 2E). Different from the water islands grown on the graphene, the honeycomb water lattices at the two sides of the boundary had exactly the same orientation. When the hBN lattice was superimposed on the water island in the same AFM image (Fig. 2F), we found good structural commensurability between the water island and the underlying hBN lattice: one B-N tetradecagon made of four B atoms and four N atoms matched well to one water hexagon (Fig. 2F and fig. S6). Because there was a small lattice mismatch of ~2.1% between the 2D water islands and the hBN (table S1), the boundary structure was necessary for releasing the strain induced by the lattice mismatch.

By performing fast Fourier transform (FFT) on the 2D water and the graphene and hBN (Fig. 2G), we found that the length of reciprocal vectors of both substrates was about two times larger than that of the 2D water. For the 2D water on the graphene, there were two sets of FFT spots for the water lattices, which were rotated by 30° with respect to each other. One set of water lattices had the similar orientation as the graphene lattice but with a small deviation (~2.5°). Therefore, both sets of water lattices were incommensurate with the graphene substrate. By contrast, there was only one set of water lattices on the hBN substrate, showing the same orientation as the hBN lattice and good commensurability. The different commensurability between the water islands and the two substrates could be quantitatively evaluated by measuring the distance between the center of the water hexagon and the centers of the nearest-neighboring C and the B-N hexagons (Fig. 2H, figs. S7 and. S8, and supplementary text). The statistical results showed that there was no characteristic distance between the water and C hexagons, but for the water and B-N hexagons, there existed a characteristic peak around 1.05 to 1.20 Å in the distance distribution, further confirming that the water lattice was incommensurate with the graphene substrate but commensurate with the hBN substrate.

Theoretical analysis of the origin of the different commensurability

Considering that the graphene and hBN surfaces have a minute lattice difference of ~1.8% and similar contact angles of water droplets (similar hydrophobicity), the different registry behavior of the water islands with the two substrates was rather unexpected. To gain deeper insight, we performed systematic density functional theory (DFT) calculations on the two systems. Figure 3A shows different adsorption configurations of the 2D water layers on the graphene (top insets) and the hBN (bottom insets) (fig. S9). All the water layers were made to be commensurate with the substrate to satisfy the periodic condition, but the adsorption sites were different for each type of water layer. Calculated binding energies of the different 2D water configurations were summarized in Fig. 3A (tables S2 and S3), showing that it was difficult to identify the preference adsorption site for the 2D water on the graphene within the DFT accuracy. By contrast, we calculated the average horizontal distance between the water molecule and its nearest B or N atoms for all the structures used in the DFT calculation (bottom insets, Fig. 3A). The most stable fBuh and fhuB structures (see Fig. 3 legend for structure naming convention) had obviously shorter water-B distances. Therefore, the water molecules tended to adsorb close to the B atoms of the hBN, consistent with the statistical experimental results (Fig. 3, B and C).

The energy corrugation at different sites on hBN was about two to three times larger than that on graphene. Such a difference could be attributed to the electronic effect: hBN has a heteropolar surface with a charge separation between the B and N atoms, and the charge distribution on graphene is quite uniform (fig. S10). The charge density difference of the most stable configurations of the two systems, the fhuC structure for the water-graphene and the
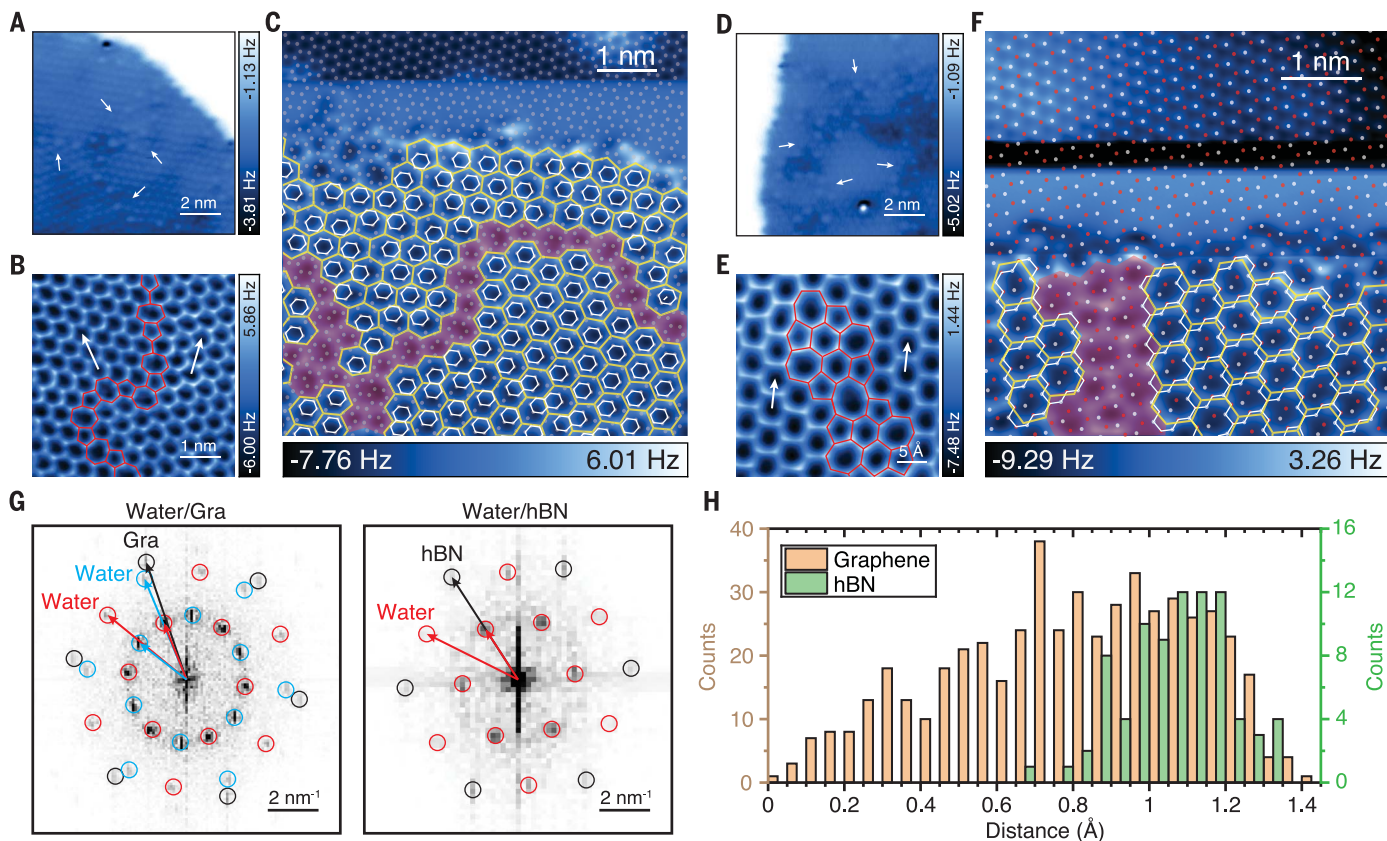
Fig. 2. Boundary structures and lattice registry of the 2D water islands on the graphene and the hBN surfaces. (**A** and **D**) Constant-height AFM images of two 2D water islands on graphene (A) and hBN (D). The arrows indicate the boundary structures. (**B** and **E**) Zoomed-in AFM images of the boundary structures in the 2D water islands, highlighted by red lines. The white arrows indicate the orientations of two domains separated by the boundary, showing angles of about 30° and 0° for the 2D water islands on graphene (B) and hBN (E), respectively. (**C** and **F**) Simultaneous AFM imaging of the 2D water islands and the substrate. The purple shadow represents the boundary region. C atoms in the graphene lattice are marked by gray dots in (C). Water and C hexagons are denoted by yellow and white lines, respectively. B and N atoms in the hBN lattice are marked by white and red dots, respectively, in (F). B-N tetradecagons marked by white lines in (F) are the simplest structural units to match the water hexagons. (**G**) FFT of the 2D water islands on graphene (left) and hBN (right). Spots of the water lattices with two different orientations on graphene are marked by red and blue circles, respectively. Spots of the water lattice on hBN are marked by red circles. Spots of the substrate lattices are marked by black circles. (**H**) Quantitative statistical results of the lattice registry for the 2D water-graphene (fig. S7) and the 2D water-hBN (fig. S8) by measuring the distance between the centers of the water hexagons and the centers of the nearest-neighboring C or B-N hexagons.

fBuh structure for the water-hBN, also showed that there was a larger charge transfer between the 2D water and the hBN (fig. S10), leading to a stronger electrostatic interaction. It has been revealed that the stability of various adsorbed water clusters was independent of the polarity of the B-N and graphene surfaces (42). Although the B-N polarization effect was not strong enough to change the structure of the 2D water, this subtle electrostatic interaction could compete with the water-water interaction, leading to lattice commensurability. On the graphene substrate, the relatively weak water-graphene interaction and the small energy corrugation resulted in the lattice incommensurability.

Measurements of friction behavior and structural superlubricity

It has been known that the atomic-scale lattice commensurability and incommensurability could affect the friction between two types of 2D materials (43–45). Although both the rotated bilayer graphene and hBN exhibited the structural superlubricity (46), the structures of water clusters were found to be closer to the hBN than the graphene sheets, exhibiting an enhanced order (47, 48). Therefore, whether the structural superlubricity exists in the 2D water systems is not straightforward owing to the low rigidity of the water structure. The manipulation of single water molecules or small clusters has been well established in the past. However, it remains a great challenge to manipulate the 2D water islands with extended hydrogen-bonding networks (>20,000 water molecules). Previous works mainly focused on the high-resolution imaging of the water hydrogen-bonding network (40, 49), but failed to manipulate the 2D water islands owing to the strong water-substrate interaction. To this end, we performed tip manipulation experiments of the 2D water islands on the graphene and hBN surfaces in a controlled manner (materials and methods) (50, 51). We chose a relatively isolated water island and laterally manipulated the water island under the constant height mode. Upon decreasing the tip height, the tip-water interaction gradually increased. At a threshold tip height, the tip-water interaction became strong enough to move the water island (Fig. 4A and fig. S11). A group of frequency shift (Δf) traces across the water island were recorded at different tip heights (Fig. 4B) from which the tip-water interaction potential could be extracted by integrating the frequency shift along the tip height twice (fig. S12 and materials and methods).

The interaction force between the tip and the water island was attractive during the manipulation process (fig. S13). In such a case, the water island was lifted up by the tip to cancel the attractive force from the substrate. Figure

Fig. 3. Binding energies of the different configurations for the 2D water islands on graphene and hBN. (**A**) Binding energies of the different configurations obtained by DFT calculation. All the structures are drawn in the supercell style of the 2D water islands, and only the water molecules in the lower layer are shown. The naming convention is based on the relative position between water molecules and substrate sites. For example, the "fhuC" structure for the 2D water on the graphene represents that the flat water molecules (f) are located on the hollow site (h) of the graphene lattice, and the H-up water molecules (u) are located on the carbon atoms (C). The "fBuN" structure for the 2D water on hBN represents that the flat water molecules (f) are located on the B atoms (B), and the H-up water molecules (u) are located on the N atoms (N). The "shift" structure represents that there is a shift between the water lattice and the substrate lattice. The average horizontal distances between the O atoms of the water molecules and their nearest-neighboring B or N atoms are shown above the

structure. (**B**) Distance measurement of the nearest-neighboring water-B and water-N. B and N atoms are indicated by white and red dots, respectively. Water hexagons are denoted by yellow lines. The distance between the O atoms of the water molecules and the nearest-neighboring B or N atoms is represented by white or red lines. (**C**) Statistics of the nearest-neighboring water-B and water-N distance in three different regions. The red dashed lines represent the average values, indicating that the water molecules tend to adsorb near the B sites rather than the N sites.
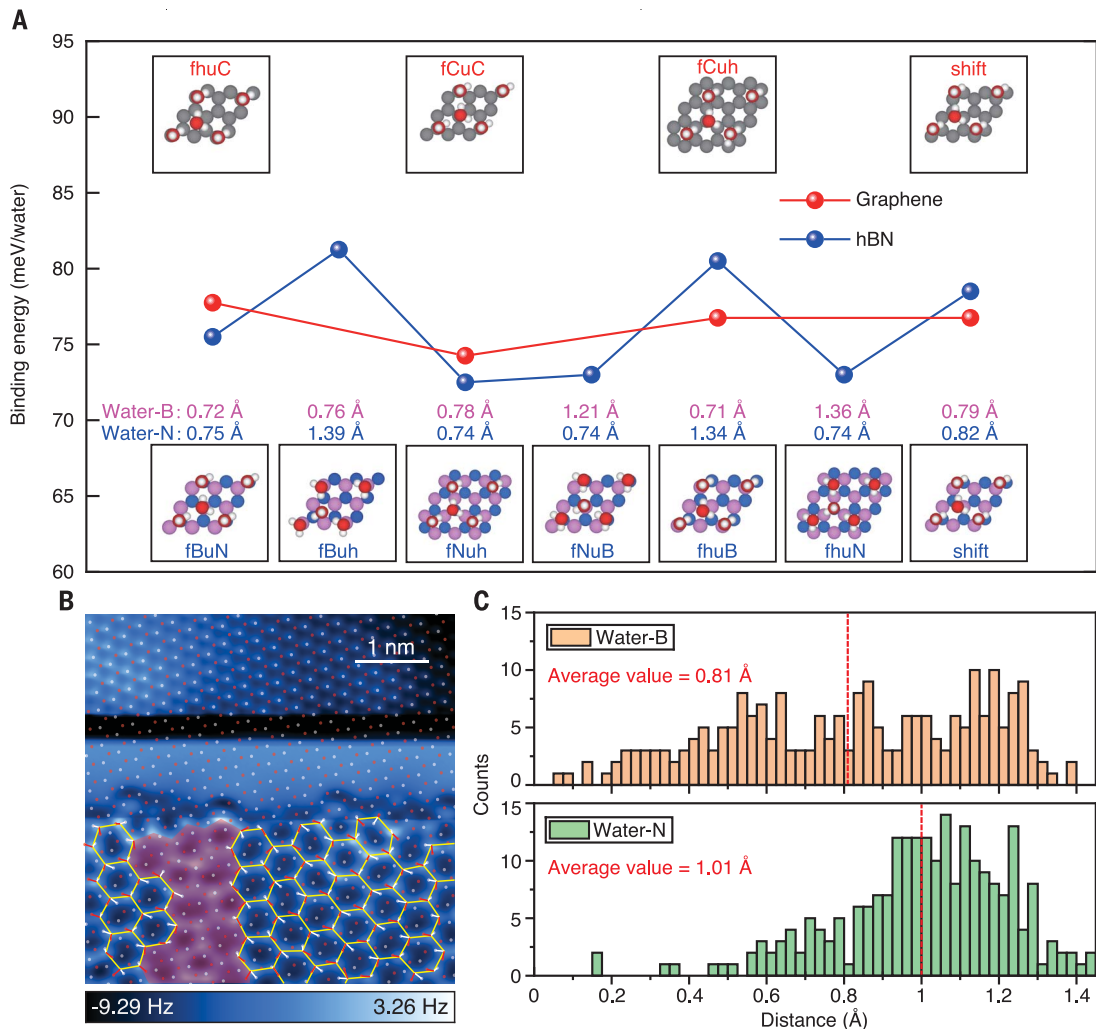
4C shows the threshold tip-water interaction potential needed to move the water islands, the lateral gradient of which gives the static friction (*52, 53*). At the threshold tip height, the tip-water friction should be equal to the water-substrate friction: $\Delta E_{t-w}/a_{t-w} = \Delta E_{w-s}/a_0$, where ΔE_{t-w} and ΔE_{w-s} are the potential corrugations at the tip-water and water-substrate interfaces, a_{t-w} is the characteristic length of the potential corrugation between the tip and the water, and a_0 is the period of the potential corrugation between the water and the substrate. For simplicity, we used the lattice constant of the substrate as a_0. Considering that the a_{t-w} was at least one order of magnitude larger than the a_0, the ΔE_{t-w} was much larger than the ΔE_{w-s}. On the other hand, in the static friction condition, we had the intrinsic potential corrugation $\Delta E_{w-s}^{in} = \Delta E_{w-s} + \Delta E_{t-w}$, assuming tip dissipation was negligible. Therefore,

we could use the threshold tip-water potential corrugation to approximate the intrinsic potential corrugation at the water-substrate interface in the absence of the tip.

From the double-log scale plot, it was clear that the measured potential corrugation (ΔE_{t-w}) followed a power (α) law as a function of island area (A) (Fig. 4D). The plot of the water and graphene showed a power of ~0.5, suggesting that the threshold potential roughly scaled with the perimeter of the water island. The intrinsic maximum static friction force at the water-substrate interface could be then estimated by $F_x = \Delta E_{w-s}^{in}/a_0 \approx \Delta E_{t-w}/a_0$. The area-normalized static friction force of the water on graphene decreased with increasing area as $F_x' \propto A^{-0.58}$ (red dashed line, Fig. 4E), leading to nearly vanishing friction (~1 pN/nm²) for the large 2D water islands. Such behavior is consistent with the so-called superlubricity

(ultralow-friction transport) (*45, 51–54*). By contrast, the threshold potential for moving the 2D water islands on the hBN was proportional to the island area (power of ~1), and the normalized static friction force (18.8 ± 4.6 pN/nm²) was insensitive to the area (blue dashed line, Fig. 4E), corresponding to the conventional friction behavior (*38*).

For comparison, molecular dynamic (MD) simulations were performed to calculate the maximum static friction force and the friction coefficient of the 2D water islands sliding laterally on the graphene or hBN substrates. The simulation results are presented in Fig. 4F, which shows a consistent trend with the experimental results (Fig. 4E). For the incommensurate water-graphene system, the normalized maximum static friction force also decreased to less than 1 pN/nm² with a power of -0.45, and the friction coefficient reduced to less than
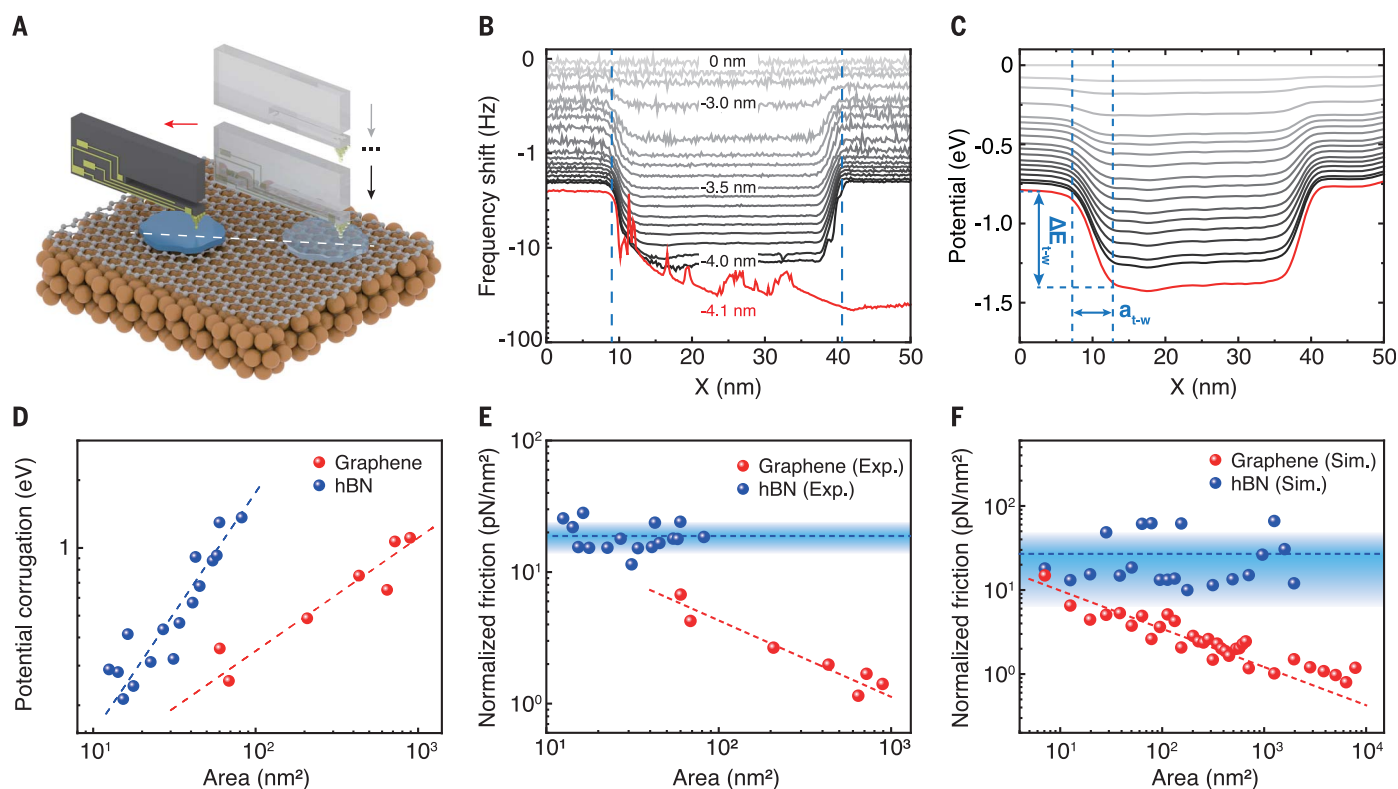
Fig. 4. Tip manipulation and deduced static friction behavior of the 2D water islands on graphene and hBN. (**A**) Schematic of the tip manipulation of a 2D water island on the graphene substrate. The tip is attached to the cantilever of a qPlus sensor. The black arrows represent multiple manipulation processes with decreasing tip height. The red arrow represents the manipulation direction. The white dashed line represents the manipulation trajectory. (**B** and **C**) Curves of frequency shift (B) and tip-sample attractive interaction potential (C) along the lateral manipulation trajectory at different tip heights. The red curves represent the threshold of 2D water sliding. The tip heights are partially marked next to the curves in (B). The blue dashed lines in (B) denote the edges of the water island. The potential corrugation and its characteristic length are denoted as $\Delta E_{t\text{-}w}$ and $a_{t\text{-}w}$, respectively [as marked by blue dashed lines and double arrows in (C)]. (**D**) Experimental threshold tip-water interaction potential (potential corrugation $\Delta E_{t\text{-}w}$) as a function of the island area. The dashed lines represent the linear fits. The slopes of the blue and red dashed lines are 1.07 and 0.50, respectively. (**E**) Area-normalized maximum static friction force of water sliding on the graphene or hBN substrates as a function of the island area obtained from the experiments (exp.). The red dashed curve represents the power law fitting of the graphene data with a power of −0.58. The blue dashed line denotes the average of the hBN data points (18.8 pN/nm²), and the blue shadow represents the standard deviation (4.6 pN/nm²). (**F**) Area-normalized maximum static friction force of water sliding on the graphene or hBN substrates as a function of the island area obtained from the MD simulations (sim.). The red dashed curve represents the power law fitting of the graphene data with a power of −0.45. The blue dashed line denotes the average of the hBN data points (26.9 pN/nm²), and the blue shadow represents the standard deviation (20.4 pN/nm²).

0.01 for the large 2D water islands (fig. S14), further confirming the superlubricity behavior (55). In contrast, for the completely commensurate water-hBN system, both the normalized friction force and friction coefficient were insensitive to the contact area. By adjusting the lattice constant of the hBN substrate, we constructed a partially commensurate case with a lattice mismatch of ~5.6% between the 2D water island and the hBN substrate (fig. S15). The normalized friction force and the friction coefficient were found to have a slightly downward trend. These results emphasized that the change of commensurability would have a remarkable impact on the friction behavior of the 2D water.

Discussion

The static friction of the 2D water island on the graphene mainly arose from the edge of the island, where an appreciable number of dangling hydrogen bonds were present. The friction of the interior island almost vanished owing to the lattice incommensurability. For the 2D water on the hBN, the friction was dominated by the majority of the water molecules inside the water island because of the lattice commensurability, and the edge molecules only played a role for small islands (area < 12 nm²) (fig. S16 and supplementary text). The measured friction (~pN/nm²) corresponds to a shear stress in the range of megapascals, which is comparable to the low-friction 2D material systems.

This work not only provided the first experimental evidence for the structural superlubricity (54) of the low-dimensional water transport to the best of our knowledge but also highlighted its sensitivity to the subtle change of the surface electrostatics. Under atomic-scale confinement, the structural order and rigidity of the water are greatly enhanced (29–34). In such a case, the water transport is related to the solid-on-solid friction, and the lattice registry between the ice-like water and the confining wall could play a decisive role in the water friction. We note that the entropic effect may lead to finite lifetimes of those icelike phases at ambient conditions. As long as the lifetimes are comparable to the timescales of the water transport, the findings in this work could be still applicable. In addition, we found that the commensurability of the 2D water can be fine-tuned by stacking the graphene on the hBN, which provides a new route toward atomic-precision engineering of the water friction and transport by the layer stacking of homopolar and heteropolar 2D materials.

REFERENCES AND NOTES

1. G. Hummer, J. C. Rasaiah, J. P. Noworyta, *Nature* **414**, 188–190 (2001).
2. M. Majumder, N. Chopra, R. Andrews, B. J. Hinds, *Nature* **438**, 44–44 (2005).
3. J. K. Holt *et al.*, *Science* **312**, 1034–1037 (2006).
4. M. Whitby, N. Quirke, *Nat. Nanotechnol.* **2**, 87–94 (2007).
5. E. Secchi *et al.*, *Nature* **537**, 210–213 (2016).
6. R. R. Nair, H. A. Wu, P. N. Jayaram, I. V. Grigorieva, A. K. Geim, *Science* **335**, 442–444 (2012).
7. H. Sui, B. G. Han, J. K. Lee, P. Walian, B. K. Jap, *Nature* **414**, 872–878 (2001).
8. X. Wang *et al.*, *Nat. Commun.* **13**, 266 (2022).
9. R. B. Schoch, J. Y. Han, P. Renaud, *Rev. Mod. Phys.* **80**, 839–883 (2008).
10. B. Radha *et al.*, *Nature* **538**, 222–225 (2016).
11. R. H. Tunuguntla *et al.*, *Science* **357**, 792–796 (2017).
12. Q. Xie *et al.*, *Nat. Nanotechnol.* **13**, 238–245 (2018).
13. Z. Zhu, D. Wang, Y. Tian, L. Jiang, *J. Am. Chem. Soc.* **141**, 8658–8669 (2019).
14. L. Bocquet, *Nat. Mater.* **19**, 254–256 (2020).
15. D. Cohen-Tanugi, J. C. Grossman, *Nano Lett.* **12**, 3602–3608 (2012).
16. S. P. Surwade *et al.*, *Nat. Nanotechnol.* **10**, 459–464 (2015).
17. J. R. Werber, C. O. Osuji, M. Elimelech, *Nat. Rev. Mater.* **1**, 16018 (2016).
18. H. B. Park, J. Kamcev, L. M. Robeson, M. Elimelech, B. D. Freeman, *Science* **356**, eaab0530 (2017).
19. B. E. Logan, M. Elimelech, *Nature* **488**, 313–319 (2012).
20. H. G. Park, Y. Jung, *Chem. Soc. Rev.* **43**, 565–576 (2014).
21. K. Falk, F. Sedlmeier, L. Joly, R. R. Netz, L. Bocquet, *Nano Lett.* **10**, 4067–4073 (2010).
22. A. Keerthi *et al.*, *Nat. Commun.* **12**, 3092 (2021).
23. C. R. Woods *et al.*, *Nat. Phys.* **10**, 451–456 (2014).
24. H. Li, X. C. Zeng, *ACS Nano* **6**, 2401–2409 (2012).
25. G. Tocci, L. Joly, A. Michaelides, *Nano Lett.* **14**, 6872–6877 (2014).
26. F. L. Thiemann, C. Schran, P. Rowe, E. A. Müller, A. Michaelides, *ACS Nano* **16**, 10775–10782 (2022).
27. A. Maali, T. Cohen-Bouhacina, H. Kellay, *Appl. Phys. Lett.* **92**, 053101 (2008).
28. X. Wen *et al.*, *Nat. Commun.* **13**, 5690 (2022).
29. N. Giovambattista, P. J. Rossky, P. G. Debenedetti, *Phys. Rev. Lett.* **102**, 050603 (2009).
30. K. Xu, P. Cao, J. R. Heath, *Science* **329**, 1188–1191 (2010).
31. P. Bampoulis, V. J. Teernstra, D. Lohse, H. J. W. Zandvliet, B. Poelsema, *J. Phys. Chem. C Nanomater. Interfaces* **120**, 27079–27084 (2016).
32. L. Fumagalli *et al.*, *Science* **360**, 1339–1342 (2018).
33. G. Algara-Siller *et al.*, *Nature* **519**, 443–445 (2015).
34. H. T. Chin *et al.*, *Nat. Commun.* **12**, 6291 (2021).
35. F. J. Giessibl, *Rev. Sci. Instrum.* **90**, 011101 (2019).
36. K. Koga, X. C. Zeng, H. Tanaka, *Phys. Rev. Lett.* **79**, 5262–5265 (1997).
37. K. Koga, H. Tanaka, X. C. Zeng, *Nature* **408**, 564–567 (2000).
38. G. He, M. H. Müser, M. O. Robbins, *Science* **284**, 1650–1652 (1999).
39. F. Schulz *et al.*, *ACS Nano* **12**, 5274–5283 (2018).
40. R. Ma *et al.*, *Nature* **577**, 60–63 (2020).
41. J. Peng *et al.*, *Nat. Commun.* **9**, 122 (2018).
42. Y. Maekawa, K. Sasaoka, T. Yamamoto, *Appl. Phys. Express* **12**, 115001 (2019).
43. M. Dienwiebel *et al.*, *Phys. Rev. Lett.* **92**, 126101 (2004).
44. Y. Song *et al.*, *Nat. Mater.* **17**, 894–899 (2018).
45. M. Liao *et al.*, *Nat. Mater.* **21**, 47–53 (2022).
46. T. Kabengele, E. R. Johnson, *Nanoscale* **13**, 14399–14407 (2021).
47. M. C. Gordillo, J. Martí, *J. Phys. Condens. Matter* **22**, 284111 (2010).
48. A. Kayal, A. Chandra, *J. Phys. Chem. C Nanomater. Interfaces* **123**, 6130–6140 (2019).
49. O. Björneholm *et al.*, *Chem. Rev.* **116**, 7698–7726 (2016).
50. M. Ternes, C. P. Lutz, C. F. Hirjibehedin, F. J. Giessibl, A. J. Heinrich, *Science* **319**, 1066–1069 (2008).
51. S. Kawai *et al.*, *Science* **351**, 957–961 (2016).
52. D. Dietzel, M. Feldmann, U. D. Schwarz, H. Fuchs, A. Schirmeisen, *Phys. Rev. Lett.* **111**, 235502 (2013).
53. S. Y. Krylov, J. W. M. Frenken, *Phys. Status Solidi, B Basic Res.* **251**, 711–736 (2014).
54. O. Hod, E. Meyer, Q. Zheng, M. Urbakh, *Nature* **563**, 485–492 (2018).
55. C. Matta *et al.*, *Phys. Rev. B Condens. Matter Mater. Phys.* **78**, 085436 (2008).
56. Z. Zhao *et al.*, Probing structural superlubricity of two-dimensional water transport with atomic resolution, version 1, Zenodo (2024); https://doi.org/10.5281/zenodo.10899937.